doi: 10.1063/5.0139501

Interplay between size and softness in the vascular dynamics of microcarriers

Wei Chien,[1] Dmitry A. Fedosov,[2] and Paolo Decuzzi[1,a)]

AFFILIATIONS

[1]Laboratory of Nanotechnology for Precision Medicine, Fondazione Istituto Italiano di Tecnologia, Genova, Italy
[2]Theoretical Physics of Living Matter, Institute of Biological Information Processing and Institute for Advanced Simulation, Forschungszentrum Jülich, Jülich, Germany

[a)]Author to whom correspondence should be addressed: paolo.decuzzi@iit.it

ABSTRACT

The geometry and mechanical properties of blood-borne particles play a major role in determining their vascular behavior and ability to evade immune cell sequestration. Within this context, the transport dynamics of deformable microcarriers (MCs) in a red blood cell (RBC) suspension is systematically investigated. Trajectories and the margination propensity of nominally spherical particles with five different diameters ($D_{MC} = 0.5$, 1, 2, 3, and 4 μm) and three levels of deformability (stiff, soft, and extra soft) are studied for two different vessel calibers (capillary: 10 μm; arteriole: 50 μm) under three different hematocrits ($H_{ct} = 10\%$, 20%, and 30%). The multi-component suspension is modeled as elastic membranes and elastic solids representing RBC and MC, respectively, immersed in Newtonian fluid simulated by smoothed particle hydrodynamics method. The results document the existence of two regimes: (i) a "collision force" regime where fast-moving RBCs push sufficiently small particles toward the wall; (ii) a "lift force" regime where sufficiently large particles migrate away from the wall. Between these two regimes, a maximum in margination propensity appears, which depends on the particle size, deformability, and flow conditions. For the considered vessel calibers and hematocrits, 2 μm MC offers the highest margination propensity. The vascular dynamics of small MC ($D_{MC} \leq 0.5$ μm) is hardly influenced by their deformability, whereas extra soft MCs behave similarly to RBCs. In addition to the limitations related to the two-dimensional analysis, these simulations suggest that moderately deformable micrometric carriers would more efficiently marginate and seek for vascular targets in the microcirculation.

I. INTRODUCTION

The transport properties of blood-borne nano/microparticles play an important role in the systemic delivery of therapeutic and imaging agents. Their effective delivery and accumulation at diseased sites require the engineering of carriers that could avoid recognition by cells of the immune systems, mostly residing within filtering organs (liver and spleen), and navigate in proximity of the blood vessel walls sensing for lumen biophysical abnormalities, such as the expression of specific vascular receptors (docking sites) or the occurrence of intra/inter-endothelial cell openings (fenestrations).[1–4] In addition, vascular carriers must modulate, and possibly exploit, the interaction with the far more abundant red blood cells (RBCs) that inevitably would affect their vascular dynamics. Specifically, RBCs are deformable, non-spherical microscopic (7 μm) corpuscles occupying a significant portion of the vascular volume, amounting to 10%–30% in the microcirculation and up to 50% in the macrocirculation. Because of their deformability, RBCs lift away from the vessel walls and tend to accumulate in the core of the blood vessels, which is characterized by higher velocities, leaving a so-called cell free layer (CFL) in proximity of the lumen.[5–8] Notably, the fast and dense layer of RBCs populating the core of the blood vessels is instrumental to a variety of biophysical processes, including the margination and extravasation of circulating leukocytes at sites of inflammation[9–11] as well as the deposition of platelets at sites of vascular injury.[12–14]

The transport of micro/nanoparticles is also known to be affected by the presence of RBCs. Lee and colleagues[15] were among the first investigators to document that small particles (<500 nm) would marginate less efficiently than large particles (>500 nm) toward the vessel walls in a capillary flow. This was demonstrated using a computational approach based on immersed finite element methods and confirmed by intravital video microscopy analyses, showing that small particles mix and move with the blood cells whereas large particles are pushed laterally toward the lumen by the same RBCs. Other authors have also shown that carriers of 200 nm, or smaller, tend to be distributed

randomly within a blood vessel, while large particles (>500 nm) exhibit a strong tendency to marginate.[16] Moreover, Charoenphol *et al.*[17] showed an increase in wall adhesion for sLeA-coated spheres as the particle size grew from 500 nm to 6.0 μm at a 30% and 45% hematocrit (H_{ct}). Indeed, this was limited for larger size (10.0 μm spheres) because of the direct collisions between RBCs and the adhering particles. Also, these observations are consistent with mesoscopic simulations[18,19] which showed an increase in particle accumulation near the wall with an increase in characteristic size from a few tens of nanometers to about 4 μm. Similar observations on the effect of carrier size were provided by other authors too.[20–24] Size is not the sole factor influencing the vascular dynamics of blood-borne particles. Previous studies have shown how the shape and the surface properties of a carrier could also play an important role. Indeed, non-spherical particles roll and tumble in flow crossing the streamlines, thus increasing their likelihood to marginate toward the walls as well as collide with RBCs.[20,24–26] Also, non-spherical particles can expose a larger surface to the vascular walls, thus presenting a stronger avidity toward firm adhesion under flow, for a given density of surface molecules. This was documented via theoretical calculations as well as confirmed by *in vitro* and *in vivo* studies.[17,18,24,27–30] Vahidkhah and Bagchi[20] have also demonstrated a non-trivial dependence of particle margination, wall contact, and adhesion on shape.

In addition to size, shape, surface density, and type of adhesion molecules, a fourth parameter is emerging in the rational design of blood-borne drug delivery systems: the softness of the carrier. Various laboratories have realized and tested particles with tunable mechanical properties. Among others, the group of DeSimone realized 5 μm deformable poly(ethylene glycol) (PEG) particles, showing how their blood longevity could be extended by increasing their softness.[31] The group of Mitragotri has demonstrated in multiple papers the ability of deformable RBCs to act as long-circulating carriers of therapeutic agents.[32,33] A recent study has shown that the uptake of particles by primary macrophages could be reduced by increasing the softness of the particles themselves.[34] Fish *et al.*[35] performed a systematic investigation of adhesion for different particle rigidities using poly(ethylene glycol) diacrylate (PEGDA) beads and reported nontrivial trends as a function of the flow rate. However, the particle deformation was minimal with a strain close to one percent. Furthermore, external fields (e.g., magnetic field) can be applied to steer drug delivery particles in microvessels.[36–38]

Engineering particles with a controlled size, shape, surface properties, and softness combination (referred to as 4S) is not an easy task. On the one hand, not all the fabrication techniques allow the independent modulation of these 4S properties over sufficiently wide intervals and, on the other hand, most *in vitro* and *in vivo* experiments focus on the final steps in the process of vascular particle dynamics: wall adhesion and tissue accumulation. In this complex scenario, simulations play an essential role not only in identifying the most relevant parameters via systematic analyses but also in supporting the understanding of the physical mechanisms regulating the dynamics of drug microcarriers (MC). In this work, we focus on interplay of particle size and deformability (or softness), in order to understand the importance of these two properties on the margination propensity of drug delivery carriers in microvasculature. Even though the effect of particle size on margination in blood flow is rather well investigated, the importance of particle deformability has received little attention so far. Furthermore, our study is motivated by the use of PEG-PLGA nanoconstructs,[35] which possess a porous inner structure with bulk elasticity in contrast to many membrane-based MCs, and aims to identify the opportunities as well as limitations of such particle platforms for drug delivery. To this end, we employ a mesoscopic computational model in order to analyze the behavior of small (0.5 μm) and large (4.0 μm) particles in capillaries (10 μm) and small arterioles (50 μm), under different hematocrit conditions. The deformation of the MCs (i.e., maximum strain due to particle stretching in flow) can reach 20% for the softest particle employed. We first provide details on the computational model and specific algorithms. Then, the deformation and dynamics of a single MC with bulk elasticity is considered in Poiseuille flow, followed by a systematic study of MC behavior in capillary and arteriolar flows of blood for different particle size and deformability. Larger and softer MCs tend to marginate efficiently in capillaries while smaller and stiffer MCs perform better in arterioles. The mechanisms behind this behavior are discussed in view of the simulation results.

II. THE COMPUTATIONAL MODEL

A computational model is used to predict the vascular behavior of a multicomponent suspension comprising RBCs and deformable MCs dispersed in an aqueous solution. There are four components of the model: (i) an aqueous solution treated as a Newtonian fluid and reproduced via the smoothed particle hydrodynamics (SPH) method;[39] (ii) RBCs modeled as a single layered elastic membrane;[40] (iii) MCs modeled as an elastic body;[41] and (iv) the fluid-RBC and fluid-MC coupling imposed via an immersed boundary (IB) method.[42,43] These four components are integrated into LAMMPS[44] and are described in Secs. II A–II D.

A. Smoothed particle hydrodynamics (SPH) method

The fluid flow is described by the Navier–Stokes equation which is discretized into Lagrangian particles (or discretization points) with particle number density $d_i = \sum_j W_{ij}$ and interactions via inter-particle forces. $W_{ij} = W(|\mathbf{r}_i - \mathbf{r}_j|)$ is the smoothing function defined as the quantic spline and $\rho_i = m_i d_i$. The dynamics of SPH particles after discretization of the Navier–Stokes equation is described as follows:[39]

$$m_i \ddot{\mathbf{x}}_i = \sum_j \mathbf{f}_{ij}^C + \mathbf{f}_{ij}^D + \mathbf{F}_{i,ext} \tag{2.1}$$

where $\mathbf{f}_{ij}^C$ and $\mathbf{f}_{ij}^D$ determine the pressure and viscous terms, respectively, while $\mathbf{F}_{i,ext}$ stands for an applied pressure gradient or distributed force from the immersed MCs. The exact formalism for the pressure $\mathbf{f}_{ij}^C$ and viscous $\mathbf{f}_{ij}^D$ terms is

$$\mathbf{f}_{ij}^C = \left(\frac{p_i}{d_i^2} + \frac{p_j}{d_j^2}\right) F_{ij} \mathbf{r}_{ij}, \tag{2.2}$$

$$p_i = p_0 \left[\left(\frac{d_i}{d_0}\right)^5 - 1\right], \tag{2.3}$$

$$\mathbf{f}_{ij}^D = -4\eta(\mathbf{v}_{ij} \cdot \mathbf{e}_{ij}) F_{ij} / (d_i d_j) \mathbf{e}_{ij}, \tag{2.4}$$

where the gradient of W_{ij} is expressed as $\nabla_i W_{ij} = -\mathbf{r}_{ij} F_{ij} = -(\mathbf{r}_i - \mathbf{r}_j) \cdot F(|\mathbf{r}_i - \mathbf{r}_j|)$, $\mathbf{e}_{ij}$ is the unit vector pointing along $\mathbf{r}_i - \mathbf{r}_j$, and η is the fluid viscosity. The particle pressure p_i is calculated from the state function in Eq. (2.3) with the parameter p_0, which controls fluid compressibility. d_0 and dr_{SPH} are the average number density of

the distributed SPH particles and the average interparticle distance $dr_{SPH} \sim 1/{d_0}^{1/2}$.

Despite a simple flow studied in this work, distribution deficiency and clustering of SPH particles may occur due to the $\mathbf{F}_{i,ext}$ contribution from immersed microstructures. A particle shifting algorithm is performed every time step to achieve stability in long-time simulations.[45] SPH particles are shifted according to a weighted kernel gradient $\mathbf{K}_i$, Eqs. (2.5) and (2.6) with $D_{diff} = -A \cdot {dr_{SPH}}^2$. After this modification, the velocity is corrected via velocity gradients. $A = 0.0025$, $n_s = 4$, and an upper bound $|\delta \mathbf{x}_i| < 0.5 \cdot dr_{SPH}$ are used in this work,[45]

$$\mathbf{K}_i = -\sum_j (1 + R_{ij})\, \mathbf{r}_{ij} F_{ij}/d_j, \quad R_{ij} = 0.24 \cdot \left[\frac{W(|\mathbf{r}_{ij}|)}{W(dr_{SPH})}\right]^{n_s}, \tag{2.5}$$

$$\delta \mathbf{x}_i \approx -D_{diff} \mathbf{K}_i. \tag{2.6}$$

All simulations are carried out in the incompressible limit with Mach number $Ma = \frac{u_{max}}{c} < 0.01$, where c is the velocity of the sound. Thus, the parameter p_0 in the state function in Eq. (2.3) is set as $p_0 = m \cdot d_0 \cdot c^2$. The time step used for laminar flow in this study is limited by the viscous stability and is set to be $\Delta t = 0.125 \cdot dr_{SPH} \cdot dr_{SPH}/(\eta/m \cdot d_0)$.[46] The smoothing length for SPH is set to be $r_c = 1.5 = 4.54 \cdot dr_{SPH}$, which includes around 40 neighbors around each fluid particle.

B. The deformable RBC model

RBCs are modeled as a single-layered elastic membrane[40] immersed in a fluid, as shown in Fig. 1(a). The restoring forces are applied both perpendicular to the membrane and along the membrane with components $u_{pe} = u_b + u_A$, $u_{pa} = u_{wlc} + u_{pow}$, respectively, where u_b accounts for bending compliance through each angle θ, u_{wlc} and u_{pow} reperesent nonlinear springs applied on each bond and u_A enforces conservation of the total enclosed area.

The bending energy has the form

$$u_b = k_b[1 - \cos(\theta - \theta_0)], \tag{2.7}$$

where k_b is the bending coefficient and θ is the angle between two neighboring bonds with a rest angle $\theta_0 = 0.0$ (i.e., zero spontaneous curvature) in all the simulations. This potential approximates the continuous bending energy in two dimensions $E_{c,2d} = \frac{\kappa_b}{2}\int_{Cir} H^2 d\hat{l}$, where κ_b is the membrane bending rigidity and H is the local membrane curvature. The relation between κ_b and k_b is derived using a circular geometry. The total energy of a circle with a radius R is $E_{c,2d} = \kappa_b \pi/R$. In the limit of small θ and uniform discretization $(2\pi/N_v)$, $E_b = N_v k_b[1 - \cos(\theta - \theta_0)] \sim N_v k_b \theta_2/2$. Thus, $\kappa_b = k_b \mathrm{l}_{ave}$ depends on the average bond length l_{ave}.

u_{pa} controls membrane stretching and applies a constraint on the circumference of the membrane in the two-dimension model. A worm-like chain potential is adopted $u_{wlc}(l) = \left(\frac{1}{p}\right) \cdot (l_m/4)\frac{3x^2 - 2x^3}{1-x}$, where $\mathrm{x} = \mathrm{l}/l_m$, l is the bond length and l_m is a predefined maximal spring length to limit elongation. The l_m is set to be $2.2 \cdot l_0$ with l_0 being the initial spring value, so that $\mathrm{x}_0 = l_0/l_m = 1/2.2$. This potential provides a nonlinear attractive force between two connected particles, limiting the extension of the spring. In addition, a repulsive force between two connected particles is implemented through a simple form $u_{pow} = k_p/l$, where $k_p = \frac{\mathrm{l}_0}{p}\left[\frac{1}{4(1-\mathrm{x}_0)^2} - \frac{1}{4} + \mathrm{x}_0\right]$ so that the sum of u_{wlc} and u_{pow} is minimized at $l = \mathrm{l}_0$, where the elastic forces are balanced. The corresponding Young's modulus (or linear elastic spring constant) can be computed as $Y = \mathrm{l}_0 \cdot \left(\frac{\partial^2 u_{pa}(l)}{\partial l^2}\right)|_{l=\mathrm{l}_0} = \frac{\mathrm{x}_0}{p} \cdot \left(\frac{1}{2(1-\mathrm{x}_0)^3} + 1\right) + \frac{2k_p}{\mathrm{l}_0^2}$.

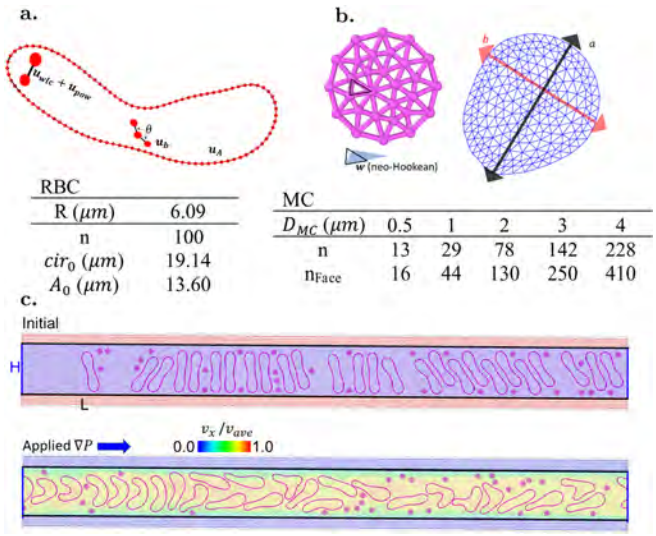

FIG. 1. Two-dimensional model of the blood flow with immersed MCs. (a) A RBC modeled as a single-layer elastic membrane with an average distance between adjacent vertices of $l_0 \sim 0.2$. The table lists the effective radius $R = C_0/\pi$ (unit of length = 1 μm), where C_0 is the RBC circumference; the area A_0 at rest; and the number n of vertices. (b) An MC modeled as an elastic patch with an average edge length of $l_{ref} \sim 0.3$. The corresponding table lists the number of vertices n and faces $\mathrm{n_{Face}}$. The deformed state is characterized by the Taylor parameter $D_{taylor} = (a-b)/(a+b)$. (c) Typical distributions of RBCs and MCs in a microchannel with a height of $H = 10$ μm and a length of $L = 120$ μm. Periodic boundary conditions are applied along the flow direction. In the initial configuration (upper image), the colormap indicates three types of particles: SPH solvent (blue), SPH wall (red) and immersed particles (pink). In the steady-flow configuration (lower image), the colormap for SPH particles indicates the velocity across the channel. Migration of particles (or margination) occurs in the direction perpendicular to the flow direction.

The incompressibility condition for the RBC cytosol (the fluid mass contained within the cell membrane) is mimicked via applying an extra constraint potential $u_A = k_A(A/A_0 - 1)^2$, where A is the total area of the cell and A_0 is the initial area. In this work, the proportion of the coefficients in the potentials implemented are set to have k_b: Yl_{ave}: k_A=1:14.1:9622. Even through the RBC model has several different energetic contributions, the shape change of RBCs is primarily dominated by the bending rigidity of the membrane κ_b, while both the circumference and the area of the RBC remain nearly constant (deviations less than 5%) in all simulations. This membrane model has been validated in our previous studies.[9,18]

C. The deformable microcarriers

Our work is motivated by PEG-PLGA drug delivery nanoconstructs, which in contrast to many membrane-based MCs, possess a porous internal structure with a bulk elasticity. Therefore, the deformable MCs are modeled as a two-dimensional neo-Hookean material,

which is similar to modeling a cell with its bulk cytoskeleton (a network of protein fibers that give shape and support to the cell). The circular patch is triangulated, and the mesh is controlled by an edge reference length l_{ref} ranging between $0.9 \cdot l_{ref}$ and l_{ref} to ensure a nearly uniform triangulation [Fig. 1(b)]. l_{ref} is set to be 0.3, which is close to the resolution of fluid with $dr_{SPH} = 0.33$. Each face is assumed to have a linearly varied displacement and a constant displacement gradient. The restoring force can be computed from a constitutive model for the areal strain energy density w and solved via a finite element method. A commonly used neo-Hookean model is adopted,

$$w = 0.5G \cdot (I_1 - 2\log J) + 0.5K \cdot (J-1)^2, \tag{2.8}$$

where $I_1 = {\lambda_1}^2 + {\lambda_2}^2 - 2$ and $J = \lambda_1\lambda_2$ are the two invariants that can be calculated from the local principal stretch ratios λ_1 and λ_2. The MC deformation is dominated by the shear modulus G with a bulk modulus K ($K = 2G$ in this work). The exact formalism for the corresponding forces and model validation are provided in Ref. 41. This model can handle large particle deformations,[42] while a simple elastic network model where only the spring forces between connected vertices are taken into account is unstable for large deformations and often exhibits nonphysical particle crumpling. Furthermore, we provide a calibration of the deformation of MCs in shear flow in Fig. S4 (supplementary material). Note that this model shows a similar behavior to membrane-based capsule or vesicle models in the regime of small deformations.

D. Fluid–structure interaction via the immersed boundary method

The immersed boundary (IB) method[43] is adopted to realize the two-way coupling between the fluid and immersed microstructures (RBCs and MCs). Microstructures move according to the velocity interpolated from the surrounding fluid, while a weighted force is transferred back to surrounding fluid particles. We use the quintic spline function as the smoothed function to solve the Navier–Stokes equation and deal with fluid–structure coupling. Recent simulations using the smoothed dissipative particle dynamics method also apply this scheme.[47] The IB scheme is applied to both RBCs and MCs. The velocity for all immersed vertices (im) i can be calculated from the interpolation of surrounding SPH particles j as follows:

$$\mathbf{v}_i^f = \frac{\sum_{j\in SPH} W_{ij}\mathbf{v}_j}{d_i}, \quad i \in im, \tag{2.9}$$

where $d_i = \sum_{j\in SPH} W_{ij}$, $i \in im$ is the number density of fluid particles surrounding the immersed vertex i. A drag force $\mathbf{f}_i^{im} = \Gamma \cdot (\mathbf{v}_i - \mathbf{v}_i^f)$ with $\Gamma = 4\pi\eta \cdot l_{ref}$ is added at every immersed vertex to transfer the momentum from fluid to immersed particles. The feedback force from RBCs and MCs to surrounding SPH particles j is calculated as follows:

$$\mathbf{f}_j = \sum_{i\in im} W_{ij} \cdot \left(\mathbf{f}_i^{im}/d_i\right), \quad \mathrm{j} \in SPH. \tag{2.10}$$

A shorter kernel length is used for fluid–structure interaction $r_c = 0.75 = 2.27 \cdot dr_{SPH}$ in this study. On average, there are ten fluid particles within the radius r_c for each vertex of the microstructures.

The resolutions of SPH fluid, RBC membrane, and MC are characterized by the average distance between fluid particles dr_{SPH}, the average edge length l_0, and the average size of the faces l_{ref}, respectively. Note that $l_0 \sim 0.2$ and $l_{ref} \sim 0.3$ are slightly less than $dr_{SPH} \sim 0.33$. In addition, to prevent overlap between different microstructures or microstructures and the wall, a short-ranged repulsive Weeks–Chandler–Anderson (WCA) potential is applied. The characteristic length of the WCA potential between different deformable particles is set to 0.15, which is related to the fluid resolution in the simulations.

E. Simulation setup

We investigate the effect of size and softness of MCs on their margination in blood flow for two microchannel sizes of H =10 and H =50 μm, mimicking capillaries and arterioles. A unit of length in our simulations corresponds to 1 μm. Several parameters of the microstructures are listed in Figs. 1(a) and 1(b). The flow of RBC-MC suspension is driven by a constant pressure gradient ($-\Delta P/L$) between two parallel planar walls using periodic boundary conditions in the flow direction [Fig. 1(c) for H =10 μm]. The flow strength is characterized by the shear rate $\dot{\gamma} = u_{ave}/H$ with $u_{ave} = (H^2/12\eta) \cdot (-\Delta P/L)$ being the mean fluid velocity in the absence of any immersed bodies. $t^* = \dot{\gamma} \cdot t$ is the dimensionless time. Fluid inertia can be neglected as the Reynolds number in the channel $Re_c = \rho u_{ave} H/\eta$ is small (see Table I).

RBC deformability with respect to applied fluid stresses is characterized by a bending-based Capillary number $Ca = \dot{\gamma}\eta R^2/(\kappa_b/R)$, which is defined as the ratio between the characteristic fluid shear stress ($\dot{\gamma}\eta$) and the elastic restoring force (κ_b/R) due to membrane bending rigidity, where R is the effective diameter of the RBC. In other words, the higher is the Ca number, the higher is the deformability of the immersed particles for given flow conditions. Ca is kept at 51.2 for $H = 10\,\mu$m corresponding to $\dot{\gamma} \sim 60\ \mathrm{s}^{-1}$ and at 110.63 for

TABLE I. Characteristic parameters for capillary ($H = 10\,\mu$m) and arteriole ($H = 50\,\mu$m) simulations considered in this work.

H (μm)		10			50	
L (μm)		120			60	
$\dot{\gamma}$ (s^{-1})		59.78			129.12	
Ca		51.22			110.63	
	Stiff	Soft	Extra soft	Stiff	Soft	Extra soft
Ca_{MC}	3.5×10^{-4}	3.5×10^{-3}	3.5×10^{-2}	4.7×10^{-4}	3.8×10^{-3}	3.8×10^{-2}
$\max(D_{talor})$	0.002–0.006	0.02–0.05	0.22–0.25	0.002–0.004	0.02–0.05	0.22–0.25
Re		0.1			3.375	

$H = 50\ \mu$m representing $\dot{\gamma} \sim 129\ s^{-1}$. For comparison, the corresponding $\dot{\gamma}$ values in three dimensions are computed as $\dot{\gamma} = Ca \cdot \kappa_{b3D}/(\eta R^3)$, taking an average value of the plasma viscosity $\eta = \eta_{plasma} = 1.2$ mPa s, a typical bending rigidity for healthy RBCs $\kappa_{b3D} = 70 k_B T$ at a temperature of 37 °C, and the effective RBC size $R = \sqrt{A/4\pi} \sim 6.51\ \mu$m with a membrane area of $A = 132.90\ \mu m^2$. Similarly, the softness of MCs is characterized by $Ca_{MC} = \dot{\gamma}\eta/G$ defined through the shear modulus G. The shape asymmetry of MCs will be characterized by the Taylor deformation parameter $D_{taylor} = (a-b)/(a+b)$, where a and b are the long and short MC axes, respectively [see Fig. 1(b)]. Note that in all simulations, no heat transfer is considered as the temperature is fixed (i.e., isothermal simulations).

III. RESULTS

The vascular transport of MCs for three different values of the shear modulus G (defined later) and five different diameters D_{MC} (500 nm, 1.0, 2.0, 3.0, and 4.0 μm) is studied in both small (a capillary with H = 10 μm) and large (an arteriole with H = 50 μm) channels. Details of the simulation conditions are listed in Table I. Note that for all simulations, RBCs and MCs are randomly distributed at time t = 0 within the aqueous solution [see Fig. 1(c)].

A. Migration of single deformable MCs in capillaries

To better understand the dynamics of multiple MCs in blood flow, it is instructive to start with the dynamics of a single, deformable carrier in the absence of RBCs. Thus, the transport of individual MCs with varying diameter D_{MC} and shear modulus G is first studied within a $H = 10\ \mu$m channel (capillary flow). In the simulations, MCs with different deformability were considered, corresponding to different capillary numbers of $Ca_{MC} = 3.5\times10^{-4}$, 3.5×10^{-3}, and 3.5×10^{-2}. These MCs will be referred to as stiff, soft, and extra soft particles further in text. Figure 2(a) shows the variation of D_{taylor} as the particle starts at a position near the wall and moves with the capillary flow driven by the externally applied pressure. During a characteristic time of $t^* \sim 1$, the deformable MC rapidly stretches (i.e., D_{taylor} grows) in response to the high shear stresses near the wall. As the MC moves further downstream, the D_{taylor} decreases, implying that the particle is exposed to progressively lower shear stresses due to its lateral migration away from the wall. Specifically, D_{taylor} reaches a maximum of ~0.22 for the extra soft MC ($Ca_{MC} = 3.5 \times 10^{-2}$), which is nearly independent of the particle size [see also the inset of Fig. 2(a) for the visualization of MC deformation]. The maximum value of D_{taylor} is approximately 0.02 and 0.002 for soft and stiff particles, respectively. Note that for $Ca_{MC} = 3.5\times10^{-4}$, the particle is very stiff but not perfectly rigid, as it still slightly deforms in flow. Figure 2(b) shows the

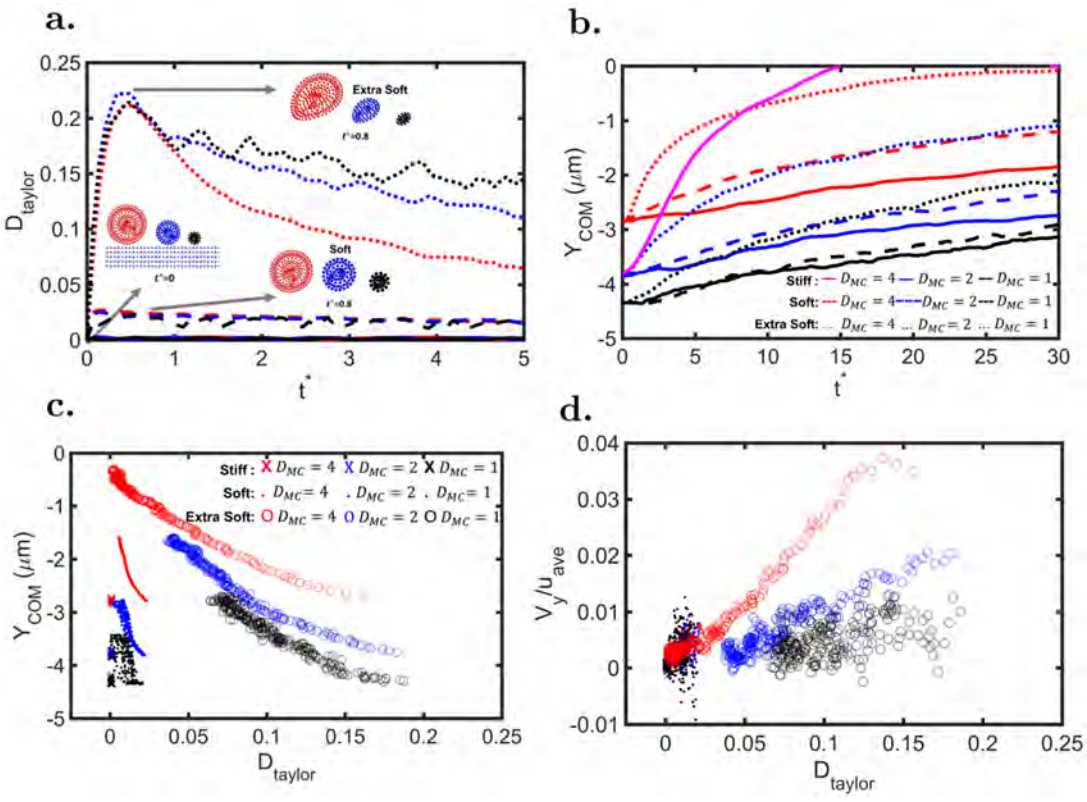

FIG. 2. Migration of individual deformable particles in a capillary flow ($H = 10\ \mu$m, $Ca = 51.22$). (a) MC deformation over time, characterized by the D_{taylor} parameter. Extra soft, soft, and stiff particles have $Ca_{MC} = 3.5\times10^{-2}$, 3.5×10^{-3}, and 3.5×10^{-4}, reespectively. The legend is the same as in plot (b). (b) Lateral trajectories of MCs over time. Pink solid line represents the migration of a single RBC at $Ca = 51.22$. (c) MC deformation as a function of its lateral position. (d) Correlation between MC lateral drift velocity V_y and deformation D_{taylor}. Symbols and their colors are the same as in the legend of plot (c).

trajectory of the center of mass (COM) Y_{COM} for each tested MC over time. As Y_{COM} also characterizes the distance of the MC center of mass from the wall along the y-axis, data in Fig. 2(b) confirm the lateral migration of MCs across the streamlines away from the wall. The migration of deformable particles away from the wall has been already extensively documented in the literatures.[7,48,49] Note that MCs with different sizes start at the same distance from the wall, so that the initial position of their COM Y_{COM} at $t^* = 0$ [Fig. 2(b)] varies with the diameter D_{MC}. Figure 2(b) also allows us to compute the migration velocity (slope of the trajectory lines) that increases with increasing MC deformability. The mechanism for cross-stream migration is attributed to the asymmetric flow field induced by the deformed particle, resulting in a lift force directed away from the wall. The variation in D_{taylor} as a function of Y_{COM} is further illustrated in Fig. 2(c). As expected, the closer is the MC to the channel axis ($Y_{COM} = 0$), the lower are the shear stresses and D_{taylor}. The MC deformation is affected by both the particle softness and size, as the latter is related to the overall stresses experienced by the particle in flow. The correlation between shape asymmetry characterized by D_{taylor} and migration velocity V_y is shown in Fig. 2(d), where V_y is proportional to D_{taylor} and positively correlates with the particle size. More accurate scaling relations can be derived by studying the effect of confinement (channel size).

For comparison, the trajectory of a single RBC starting near the wall is also shown in Fig. 2(b) (pink solid line). Indeed, given the much larger Taylor parameter for RBCs at rest ($D_{taylor} \sim 0.6$) as compared to MC ($D_{taylor} = 0$), the former experience a much faster migration away from the wall toward the center of the channel in comparison with the latter [see Figs. 2(b) and S1 (supplementary material)]. Note that the migration behavior of single MCs and RBCs in larger channels (e.g., arterioles) is similar to that in capillaries.

B. Transport of MCs in a capillary flow of blood

We begin with the transport of MCs in blood flow within a channel whose height $H = 10\ \mu m$ is comparable to the characteristic size of RBCs ($\sim 7\ \mu m$). Under a relatively strong confinement (e.g., in capillaries) and for low enough H_{ct} values, RBCs tend to organize into a single-file configuration with parachute-like shapes, in agreement with previous reports[5,8,50] (see Fig. 3). The number of MCs in the suspension is

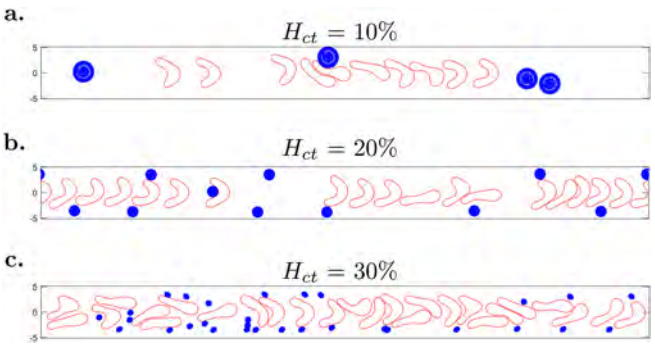

FIG. 3. Snapshots of a capillary flow at various hematocrits ($H = 10\ \mu m$, $Ca = 51.22$). (a) Suspension of RBCs with MCs at $H_{ct} = 10\%$ ($D_{MC} = 4.0\ \mu m$, $Ca_{MC} = 3.5\times10^{-4}$). (b) Suspension of RBCs with MCs at $H_{ct} = 20\%$ ($D_{MC} = 2.0\ \mu m$, $Ca_{MC} = 3.5\times10^{-3}$). (c) Suspension of RBCs with MCs at $H_{ct} = 30\%$ ($D_{MC} = 1.0\ \mu m$, $Ca_{MC} = 3.5\times10^{-2}$).

TABLE II. Total number of MCs and RBCs in the simulations of capillary flow with $H = 10\ \mu m$.

D_{MC} (μm)	No. MCs	Volume fraction (%)
0.5	63	1.03
1	30	1.96
2	11	2.88
3	6	3.53
4	4	4.19
H_{ct} (%)	No. RBCs	Volume fraction (%)
0	1	1.13
10	10	11.33
20	18	20.40
30	26	29.47%

reduced with increasing their diameter D_{MC}, so that the total area occupied by the MCs (i.e., vascular volume fraction) remains lower than 5% in all simulations. Specifically, there are 63 MCs for the case of $D_{MC} = 0.5\ \mu m$, and only 4 MCs when $D_{MC} = 4.0\ \mu m$ (see Table II).

1. MC trajectories and margination efficiency

Time-dependent trajectories of MCs immersed in a RBC suspension with $H_{ct} = 20\%$ were analyzed, starting from the extreme cases of stiff and extra soft MCs with $D_{MC} = 0.5$ and $4.0\ \mu m$ (see Fig. 4). The stiff particles almost do not deform with a $D_{taylor} < 0.01$, while the extra soft particles deform considerably, reaching values of D_{taylor} up to 0.22 near the wall [see Fig. 2(a)]. The average velocity of RBCs within the suspension (u_{RBC}) divided by the average flow velocity of the pure fluid (i.e., without RBCs and MCs) (u_{ave}) is plotted as a function of time in Fig. 4(a). For all cases with extra soft MCs, regardless of their size, and for the case with small stiff MCs, the mean velocity u_{RBC} quickly reaches a quasi-steady value of about $1.1u_{ave}$, which is similar to the case with only RBCs (no MCs) in flow. In contrast, for the case of stiff large MCs, the average RBC velocity u_{RBC} fluctuates around a significantly lower mean value of $0.85u_{ave}$. The reduced flow velocity in this case is indicative of transient increased-flow-resistance episodes in the capillary, resulting from collisions between RBCs and the stiff large MCs. Figures 4(b)–4(e) present the actual trajectories of the MCs along the capillary. Each colored line is associated with a different MC case and the thickness of the line represents the actual lateral size spanned by the MC in the y-direction while moving downstream. For the large carriers with $D_{MC} = 4.0\ \mu m$, stiff MCs accumulate next to the wall (at $Y = \pm 5\ \mu m$), as opposed to the soft MCs whose trajectories exhibit fluctuations near the capillary center (at $Y = 0\ \mu m$), as shown in Figs. 4(b) and 4(d). For the small MCs, large fluctuations in their lateral position are observed in Figs. 4(c) and 4(e). Both soft and stiff MCs spend a considerable amount of time near the wall (or equivalently marginate efficiently), with occasional crossing of the channel from one wall to the other.

To quantify margination properties of different particles, a "skin layer" with a fixed thickness of $d_{skin} = 1.0\ \mu m$ is introduced next to the walls. In Figs. 4(b)–4(e), this layer is drawn by dashed straight lines, and an MC is considered to be "marginated" when it has any

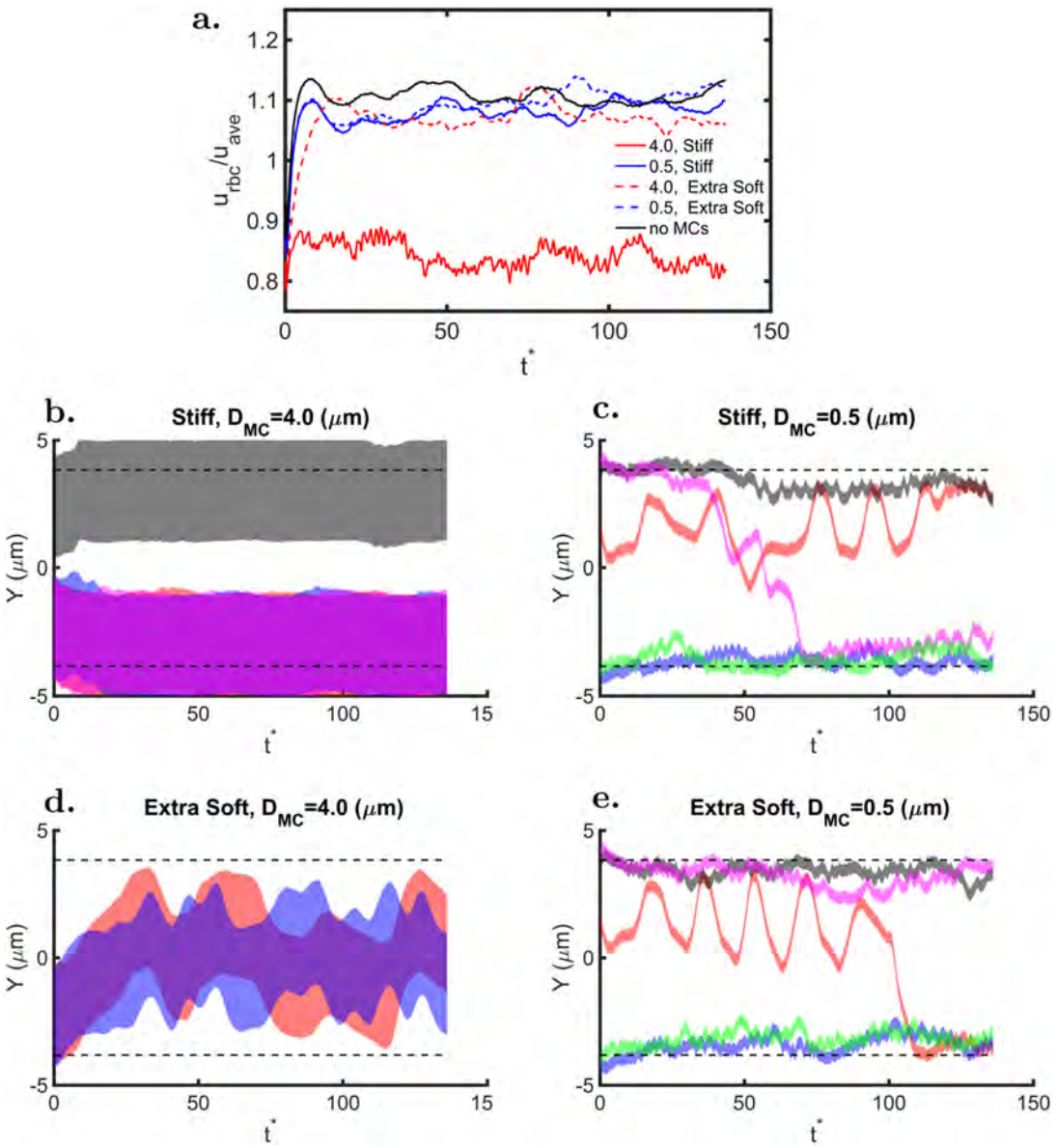

FIG. 4. Vascular dynamics of MCs in a capillary flow (H_{ct} = 20%, Ca = 51.22, H = 10 μm). (a) Average velocity of RBCs u_{rbc} normalized by the average flow velocity u_{ave} of pure fluid (i.e., without RBCs and MCs) as a function of the dimensionless time $t^* = \dot{\gamma} \cdot t$. (b)–(e) Representative trajectories of various MC types (small and large, stiff, and extra soft). The width of the lines represents the lateral size of the carrier, whereas the colors identify trajectories of different individual MCs. Selected trajectories for (b) large and stiff MCs ($D_M = 4.0\,\mu$m, $Ca_{MC} = 3.5\times10^{-4}$), (c) small and stiff MCs ($D_M = 0.5\,\mu$m, $Ca_{MC} = 3.5\times10^{-4}$), (d) large and extra soft MCs ($D_M = 4.0\,\mu$m, $Ca_{MC} = 3.5\times10^{-2}$), and (e) small and extra soft MCs ($D_M = 0.5\,\mu$m, $Ca_{MC} = 3.5\times10^{-2}$). The dashed black lines indicate the skin layer near the walls with a thickness of $d_{skin} = 1.0\,\mu$m.

intersection (even a partial overlap) with the skin layer. Then, a margination efficiency (F_M) is defined as the ratio between the number of marginated MCs having a non-zero overlap with the skin layer and the total number of MCs in the capillary. F_M is plotted in Fig. 5 for the four MC cases considered above as a function of time. Note that, $F_M = 0.0$ implies no margination, while $F_M = 1$ corresponds to the margination of all MCs. Large stiff MCs marginate toward the wall with F_M reaching rapidly the value of unity. This result is consistent with previous experimental and simulations studies,[15,18,19] which report an increase in the accumulation of rigid particles near the wall with an increase in their characteristic size. Conversely, large extra soft MCs migrate away from the wall, resulting in $F_M = 0.0$ already at $t^* \sim 10$. The two cases with small ($D_{MC} = 500$ nm) MCs show partial margination with F_M values close to 0.4 (stiff) and 0.2 (extra soft).

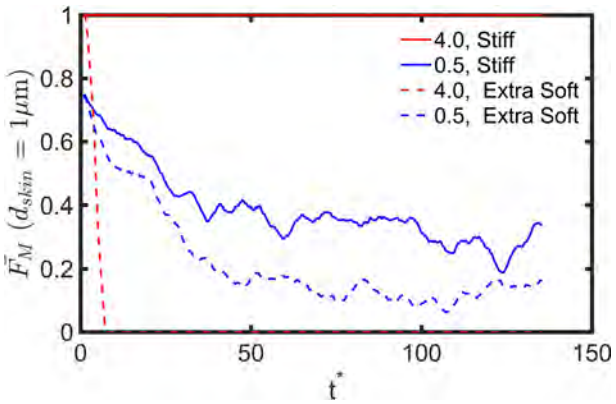

FIG. 5. Margination efficiency of MCs in a capillary flow as a function of time (H_{ct} = 20%, Ca = 51.22, H = 10 μm). Time-dependent margination efficiency F_M defined as the ratio between the number of MCs (partially) overlapping with the skin layer and the total number of MCs in the capillary. F_M = 0.0 implies no margination, whereas F_M = 1 indicates full margination. Each data point in the curves is an average over a time period of 3.45 $\dot{\gamma}^{-1}$.

Although rather small, there is also an effect of particle deformability on the margination propensity for the small MCs. Note that the thickness of the skin layer is chosen arbitrary, as in this narrow channel, it is difficult to define a CFL (a near wall layer without RBCs) properly. As discussed in the supplementary material and Fig. S2 (supplementary material), varying the thickness of the skin layer does change the values of F_M; however, the conclusions drawn above remain unaffected.

2. Analysis of the margination efficiency at different hematocrits

One of the main conclusions so far is that stiff MCs marginate better than soft MCs. In the margination process, RBC-MC interactions are fundamental, and it is therefore important to better characterize the contribution of hematocrit to the MC margination. Figure 6 shows the dependence of the average margination efficiency $\overline{F}_M$ (the average is performed after the flow has reached steady state for times $t^* > 50$) on the particle size D_{MC} (0.5, 1, 2, and 4 μm), deformability (stiff, soft, and extra soft), and hematocrit H_{ct} (10%, 20%, and 30%). Note that F_M can have strong fluctuations in time, as the number of MCs in simulations is relatively small (see Table II). Error bars in Fig. 6 correspond to the standard deviation of instantaneously measured F_M values.

At H_{ct} = 10% [Fig. 6(a)], the average margination efficiency $\overline{F}_M$ for the stiff particles (red line) increases as D_{MC} increases from 1.0 to 3.0 μm, reaching a maximum of $\overline{F}_M \sim 0.8$ for D_{MC} = 3.0 μm. Then, for D_{MC} = 4.0 μm.

At H_{ct} = 20% [Fig. 6(b)], $\overline{F}_M$ for stiff (red line) and soft (blue line) MCs increases with increasing D_{MC}, without a clear extremum for the range of simulated particle sizes. Interestingly, for both stiff and soft particles, the average margination efficiencies have comparable values, and the two curves nearly overlap. In the case of extra soft MCs (pink line), the $\overline{F}_M$ values decay with increasing D_{MC} and approach the value of zero at D_{MC} = 4 μm. Note that the margination properties of MCs at H_{ct} = 20% [Fig. 6(b)] are better than those at H_{ct} = 10% [Fig. 6(a)], evidenced by larger $\overline{F}_M$ values for the larger hematocrit.

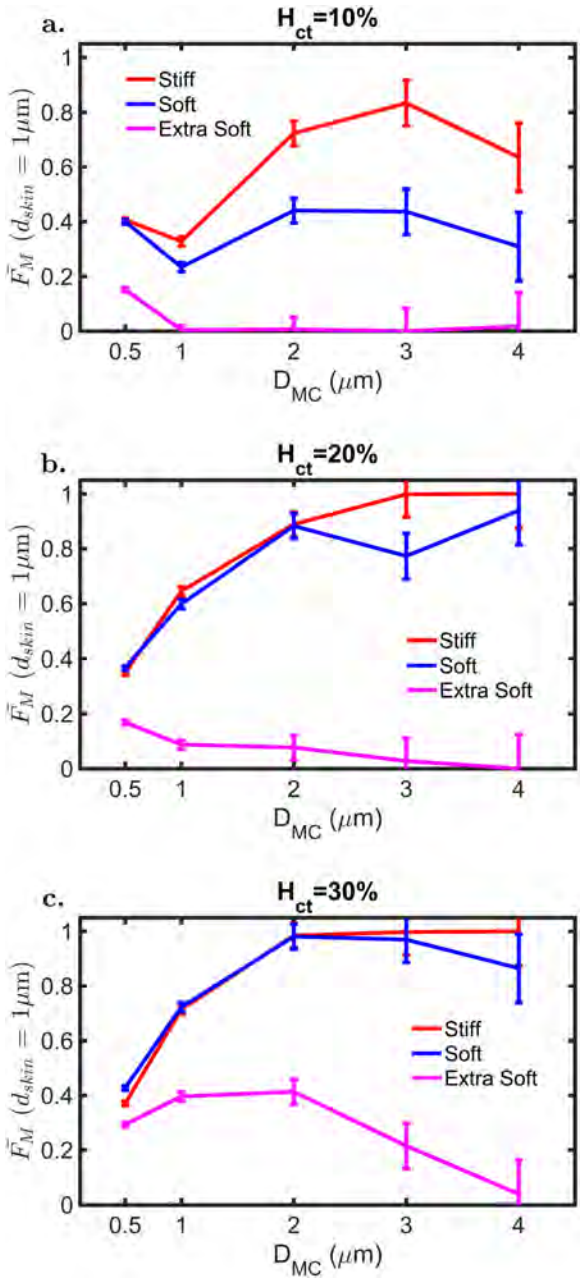

FIG. 6. Analysis of the margination efficacy at various hematocrits in a capillary flow (H = 10 μm, Ca = 51.22). Average margination efficiency $\overline{F}_M$ calculated after the flow has reached steady state, for $t^* > 50$. (a) H_{ct} = 10%, (b) H_{ct} = 20%, and (c) H_{ct} = 30%. The relative ratio of MC shear moduli is $G_{Stiff} : G_{Soft} : G_{Extra\ Soft}$ = 100 : 10:1.

Finally, at H_{ct} = 30% [Fig. 6(c)], the trends in margination propensity characterized by $\overline{F}_M$ are very similar to those for H_{ct} = 20% in Fig. 6(b). However, there is a noticeable improvement in the margination of extra soft MCs (pink line) at this hematocrit in comparison with H_{ct} = 20%.

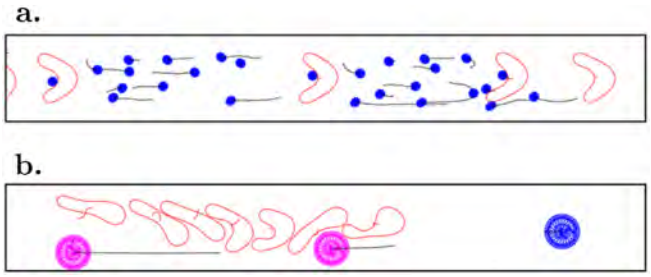

FIG. 7. Hydrodynamic effects of MCs at low hematocrits (H = 10 μm, Ca = 51.22, H_{ct} = 10%). RBCs and MCs are shown at the end of a time frame of 3.45 $\dot{\gamma}^{-1}$ after the flow converges to a steady state. The trajectories of their centers of mass within this time frame are drawn by red and black solid lines for RBCs and MCs, respectively. A frame of reference moving together with the RBCs is selected here. (a) Entrapment of small particles within the bolus flow, which develops between two RBCs moving in a train-like configuration. D_{MC} = 1.0 μm and $Ca_{MC} = 3.5\times10^{-2}$. (b) Transient increase in the flow resistance, as large MCs disturb the train-like arrangement of RBCs. D_{MC} = 4.0 μm and $Ca_{MC} = 3.5\times10^{-4}$. Multimedia views: https://doi.org/10.1063/5.0139501.1; https://doi.org/10.1063/5.0139501.2

3. Worth-mentioning hydrodynamic effects

At H_{ct} = 10%, there exist several interesting flow features, which are associated with a low-density train-like arrangement of RBCs in capillary flow. Sufficiently small and deformable MCs are frequently trapped between two neighboring RBCs in the formed cell train, while sufficiently large and stiff MCs result in recurrent disturbances to the train-like configuration of RBCs. Both of these processes are illustrated best in a frame of reference moving together with the RBCs, see Fig. 7 (Multimedia view). Shown RBCs and MCs are depicted at the end of a time frame of 3.45 $\dot{\gamma}^{-1}$, while the trajectories of their centers of mass within this time frame are drawn by red and black solid lines for RBCs and MCs, respectively. Figure 7(a) (Multimedia view) demonstrates that small MCs often become trapped within the bolus flow which develops between two adjacent RBCs. Most of the small MCs remain in the bolus flow during the whole simulation. Note that the hydrodynamic trapping can also occur temporarily for larger MCs, as shown in Fig. 7(b) (Multimedia view). Softer MCs tend to be entrapped more easily than stiff particles, due to stronger lift forces on the soft MCs. Particle entrapment within the bolus flow has also been observed in recent 3D simulations.[53] Similar trapping effects can also take place at larger hematocrits (H_{ct} > 10%), but it is generally limited to small particles.

Figure 7(b) (Multimedia view) shows the effect of large stiff MCs which frequently disturb the train-like arrangement of RBCs and lead to a transient increase in the flow resistance. Thus, stiff particles with a diameter $D_{MC} > 2.0\,\mu$m often displace RBCs away from the channel center, resulting in a temporary increase in the flow resistance until the displaced RBCs regain their position at the channel center. Furthermore, interactions between RBCs and MCs or between different MCs can lead to the demargination of MCs toward the channel center, where they become partially trapped within the bolus flow [see the blue MC in Fig. 7(b) (Multimedia view)]. This entrapment is generally transient and disappears at sufficiently large H_{ct} values.

C. Blood-flow transport of MCs in arterioles

In this section, a channel with a height of H = 50 μm is considered, which is about seven times larger than a typical RBC size and represents a typical diameter of arterioles. Similar to the previous analysis, the transport of MCs with five different diameters D_{MC} and three values of deformability (Table I) is studied in blood flow at two hematocrits (H_{ct} = 20% and 30%).

Initially at $t^* = 0$, MCs are placed uniformly across the channel, as shown in Fig. 8. After the pressure difference is applied, RBCs and MCs migrate laterally and become redistributed within the channel. Different from the case of capillary flow, where RBCs often assume a train-like configuration of parachutes, RBCs in larger channels have a less regular distribution with various shapes and orientations. Note that for H = 50 μm, the CFL can easily be identified as a near wall region depleted of RBCs, see the pink layer in Fig. 8. Similar to the case of H = 10 μm, the number of MCs is adjusted according to their size, so that the overall MC volume fraction stays below 5% in all simulations. In particular, there are 49 MCs with a 0.5 μm diameter and eight MCs with a 4.0 μm diameter, as listed in Table III.

1. MC trajectories and margination efficiency

As in the case of capillary flow, we start with well-contrasted conditions, including two particle sizes (D_{MC}=0.5 and 4.0 μm) and deformabilities (stiff and extra soft) at H_{ct} = 20%. The average RBC velocity u_{rbc} normalized by the flow velocity u_{ave} of a pure fluid (i.e., without RBCs and MCs) is plotted in Fig. 9(a) as a function of time. u_{rbc} ranges between $0.9u_{ave}$ and $1.2u_{ave}$ and is only moderately affected by different MCs. Fully developed flow is reached at around $t^* \sim 100$, during which the RBCs travel on average a length of $dx_{RBC} \approx 2500\,\mu\text{m} = 50\text{H}$, in agreement with previous studies reporting entrance lengths for the flow convergence in the range of 25–50 H.[51,52]

Individual particle trajectories are shown in Figs. 9(b)–9(e) for different MC properties. In addition, the CFL is plotted by black dashed lines, which confirm that the CFL also reaches a steady thickness δ_{CFL} at $t^* \sim 100$, consistently with the development of the flow velocity. Figure 9(b) shows that stiff MCs starting near the channel center (grey and red lines) migrate toward the wall and finally end up within the CFL. Another particle (blue line) that starts near the wall (blue) remains inside the CFL during the entire simulation. None of the stiff and large MCs are observed to reenter the core of the channel from the CFL. In contrast, large and extra soft MCs, whose trajectories are shown in Fig. 9(d), are able to explore different positions within the channel. In particular, large and extra soft MCs can escape from the CFL [see the blue trajectory in Fig. 9(d)] are migrate back into the core of the channel. The small MCs [Figs. 9(c) and 9(e)] behave similar to the large and extra soft MCs, regardless of their deformability. Visually, the frequency of reentrance of the channel core from the CFL is larger for small MCs than for large and extra soft MCs.

For the channel with H = 50 μm, we first compute the margination efficiency $F_M(d_{skin} = \delta_{CFL})$, which is defined as the number of MCs having an overlap with the CFL divided by the total number of MCs. The average thickness of the CFL at H_{ct}= 20% is equal to approximately 10 μm [Figs. 9(b)–9(e)]. The variation of $F_M(d_{skin} = \delta_{CFL})$ as a function of time is given in Fig. 10(a). For small MCs, independently whether stiff (blue line) or extra soft (pink line), the margination propensity is similar and oscillates around $F_M(d_{skin} = \delta_{CFL}) = 0.5$. However, the behavior of large MCs does depend on their deformability. Stiff MCs with D_{MC}= 4.0 μm fully marginate into

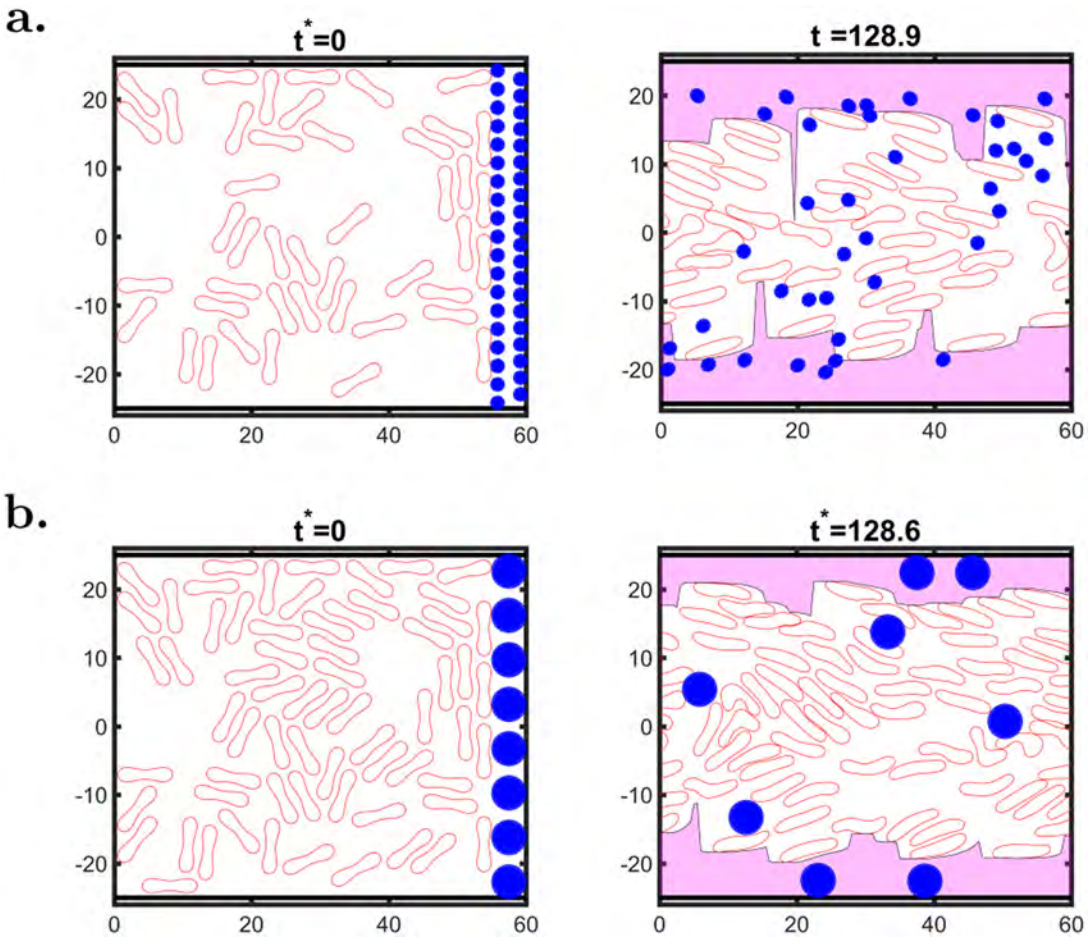

FIG. 8. Snapshots of an arteriolar flow at various hematocrits (H = 50 μm, $Ca = 110.63$). Initial configuration ($t^* = 0$) of RBCs and MCs and their distribution in arteriolar flow at $t^* \approx 129$ for (a) D_{MC}=1.0 μm and $Ca_{MC} = 3.8\times10^{-2}$ at $H_{ct} = 20\%$, and (b) D_{MC}=1.0 μm and $Ca_{MC} = 4.7\times10^{-4}$ at $H_{ct} = 30\%$. The pink layer near the wall denotes the CFL.

the CFL after $t^* \sim 350$ [i.e., $F_M(d_{skin} = \delta_{CFL}) = 1$] and remain within the CFL for the entire duration of the simulation. Differently, as already illustrated in Fig. 9(d), large and extra soft MCs do not get trapped within the CFL, resulting in $F_M(d_{skin} = \delta_{CFL}) = 0.5$. For comparison, Fig. 10(b) presents the margination efficiency $F_M(d_{skin} = 1\ \mu\text{m})$ into a 1 μm thick skin layer, as it has been used in Fig. 5 for the case of capillary flow. Here, only the large and rigid MCs present a non-zero value of $F_M(d_{skin} = 1\ \mu\text{m})$, while $F_M = 0$ in all other cases.

TABLE III. Total number of MCs and RBCs in the simulations of arteriolar flow with $H = 50\ \mu$.

D_{MC} (μm)	No. MCs	Volume fraction (%)
0.5	49	0.32
1	39	1.02
2	13	1.36
3	10	2.36
4	8	3.35
H_{ct} (%)	No. RBCs	Volume fraction (%)
30	66	29.93
20	44	19.95

2. Analysis of the margination efficiency at different hematocrits

Figure 11 presents the MC margination efficiency in the large channel with $H = 50\ \mu$m. At $H_{ct} = 20\%$, average margination efficiency $\overline{F}_M$ into the CFL [Fig. 11(a)] increases with increasing particle size for rigid and soft MCs. For extra soft MCs, $\overline{F}_M(d_{skin} = \delta_{CFL})$ is smaller than that for less deformable particles and attains a maximum for $D_{MC} \approx 2.0\ \mu$m. Margination of MCs into a 1.0 μm thick layer next to the wall is relatively weak, as shown in Fig. 11(b) by $\overline{F}_M(d_{skin} = 1\ \mu\text{m})$. Only large and stiff MCs have a non-zero average margination efficiency at $H_{ct} = 20\%$. At $H_{ct} = 30\%$ in Fig. 11(c), the trend in $\overline{F}_M(d_{skin} = \delta_{CFL})$ is less regular and appears to be similar for all MC deformabilities. Note that the errors are larger here, as longer simulation times are needed to sample the margination properties of MCs.

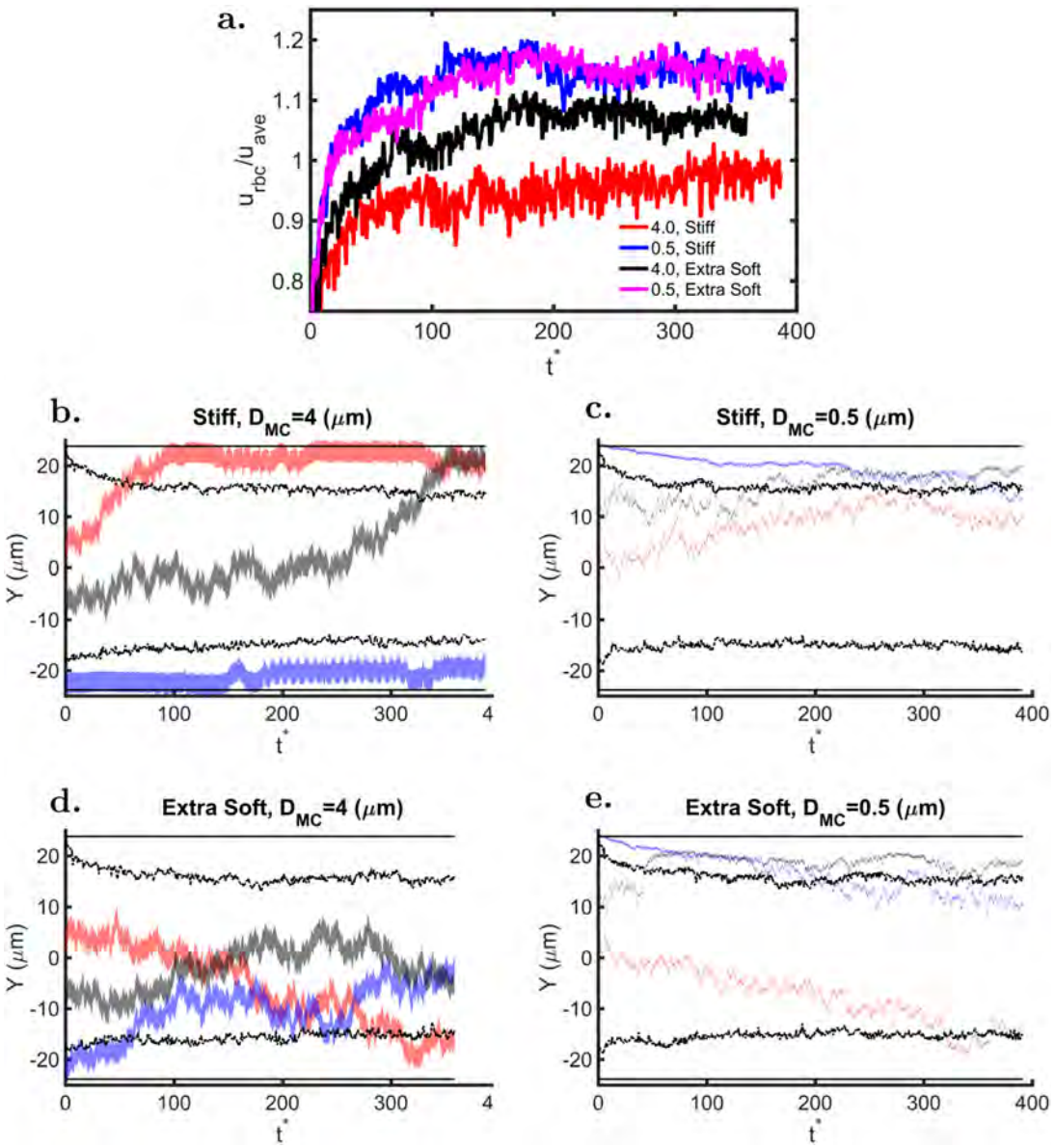

FIG. 9. Vascular dynamics of MCs in an arteriolar flow ($H_{ct} = 20\%$, Ca = 110.63, H = 50 μm). (a) Average velocity of RBCs u_{rbc} normalized by the average flow velocity u_{ave} of pure fluid (i.e., without RBCs and MCs) as a function of the dimensionless time $t^* = \dot{\gamma} \cdot t$. (b)–(e) Representative trajectories of various MC types (small and large, stiff, and extra soft). The width of the lines represents the lateral size of the carrier, whereas the colors identify trajectories of different individual MCs. Selected trajectories for (b) large and stiff MCs ($D_M = 4.0\,\mu$m, $Ca_{MC} = 4.7\times10^{-4}$), (c) Small and stiff MCs ($D_M = 0.5\,\mu$m, $Ca_{MC} = 4.7\times10^{-4}$), (d) Large and extra soft MCs ($D_M = 4.0\,\mu$m, $Ca_{MC} = 3.8\times10^{-2}$), and (e) small and extra soft MCs ($D_M = 0.5\,\mu$m, $Ca_{MC} = 3.8\times10^{-2}$). The time-dependent black dashed lines indicate the average location of the CFL, while the solid black lines correspond to the skin layer of $d_{skin} = 1.0\,\mu$m.

To ensure that the flow is fully developed, the sampling of $\overline{F}_M$ has been started after $t^* \approx 400\ \dot{\gamma}^{-1}$. Figure S3 (supplementary material) also presents margination efficacy measured at different time points in the arteriolar flow and confirms that computed values of $\overline{F}_M$ do not significantly change in time after the flow has converged to the steady state. For all MC rigidities, $\overline{F}_M(d_{skin} = \delta_{CFL})$ reaches a maximum for $D_{MC} \approx 2.0$–$3.0\ \mu$m. Figure 11(d) shows that $\overline{F}_M(d_{skin} = 1\,\mu\text{m})$ is not zero only for large and stiff enough MCs, in agreement with the results in Fig. 11(b) for $H_{ct} = 20\%$.

IV. DISCUSSION

A. Dynamics of deformable MCs in blood flow

Simulation results in Figs. 6 and 11 document the dependence of the margination propensity $\overline{F}_M$ of particles on both their size D_{MC} and

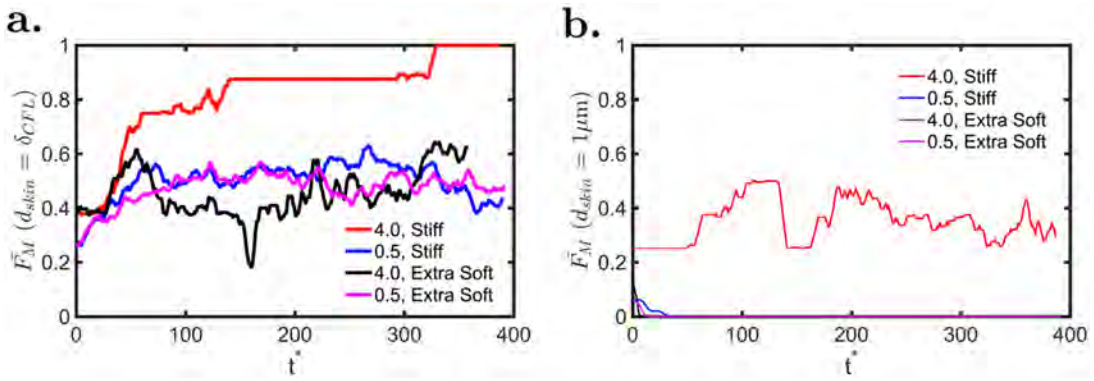

FIG. 10. Margination efficiency of MCs in an arteriolar flow as a function of time ($H_{ct} = 20\%$, Ca = 110.63, H = 50 μm). (a) Time-dependent margination efficiency inside the CFL with a thickness δ_{CFL}. (b) Time-dependent margination efficiency inside the skin layer with $d_{skin} = 1.0$ μm. The margination efficiency $F_M = 0.0$ implies no margination, whereas $F_M = 1$ indicates full margination. Each data point in the curves is an average over a time period of 7.76 $\dot{\gamma}^{-1}$.

deformability. In general, a maximum in the margination efficiency as a function of MC size is observed. Thus, F_M increases with the particle size, reaches a maximum value, and then decreases for large MC sizes. The maxima are affected by the hematocrit and particle deformability.

This unique behavior of the MCs can be understood by considering that particle margination is governed by the fine balance between two forces: (i) lift force resulting from hydrodynamic interactions between deformed non-spherical particles and the wall, and (ii) collision force due to direct interactions between the fast moving RBCs and the MC.[18,19,48] Indeed, the both forces are affected by the MC size and deformability. For example, larger and stiffer particles experience small lift forces due to their limited deformability, and more energetic collisions with RBCs determining their rapid margination toward the wall. This can be identified as a RBC collision force dominated regime.

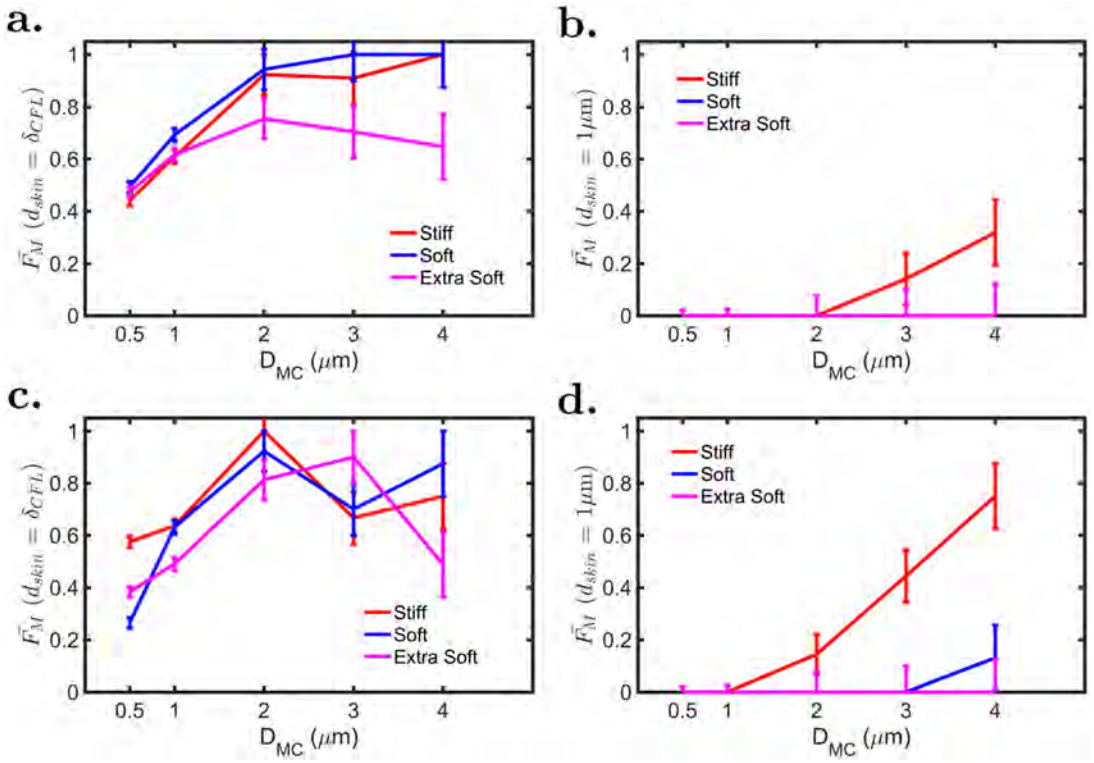

FIG. 11. Analysis of the margination propensity at various hematocrits in an arteriolar flow (H = 50 μm, Ca = 110.63). Average margination efficiency $\overline{F}_M$ calculated after the flow has reached steady state, for $t^* > 400$. (a) $\overline{F}_M(d_{skin} = \delta_{CFL})$ and (b) $\overline{F}_M(d_{skin} = 1\,\mu\text{m})$ in a RBC suspension at $H_{ct} = 20\%$. (c) $\overline{F}_M(d_{skin} = \delta_{CFL})$ and (d) $\overline{F}_M(d_{skin} = 1\,\mu\text{m})$ at $H_{ct} = 30\%$. The relative ratio of MC shear moduli is $G_{stiff} : G_{Soft} : G_{Extra\,Soft} = 80 : 10 : 1$.

In capillaries (Fig. 6) at $H_{ct} = 10\%$, stiff particles present a maximum $\overline{F}_M$ of 0.8 for $D_{MC} = 3.0\ \mu$m. For soft particles, the maximum margination propensity reduces to $\overline{F}_M = 0.4$ found for similar values of $D_{MC} = 2.0$ and 3.0 μm. At larger hematocrits, the collision force dominated regime becomes even clearer. At $H_{ct} = 20\%$ and 30%, stiff and soft MCs present maxima of $\overline{F}_M \sim 1.0$ for $D_{MC} = 2.0$ and 3.0 μm. Note that the decrease in margination propensity at large MC sizes ($D_{MC} > 3.0\ \mu$m) has to be ascribed to the effect of the lift force. As the particle size and deformability increase, the lift force becomes more dominant than the contribution of the collision force. This can be identified as a lift force dominated regime. For instance, the lift force on the extra soft MCs (pink lines) is large, preventing their margination. In fact, these particles behave similar to RBCs and, at sufficiently low hematocrits, can easily access the space between two adjacent RBCs and accumulate close to the center of the channel. At larger H_{ct} (>20%), however, the train of RBCs becomes more compact and the collision force dominates over the lift force for the smaller extra soft particles. The modest discrepancies from the described behavior (e.g., at $H_{ct} = 10\%$ for the smaller particles and at $H_{ct} = 20\%$ for the soft MCs with $D_{MC} = 3.0\ \mu$m) should be associated with statistical errors.

The same margination mechanisms also apply to the larger vessels, for which the margination behavior is depicted in Fig. 11. In addition to moderate fluctuations in the values of the margination efficiency, which are mostly related to statistical errors, the trend of $\overline{F}_M$ with D_{MC} is also clearly observed in arterioles for different MC deformability. At $H_{ct} = 20\%$, stiff and soft particles present a maximum of $\overline{F}_M \sim 1.0$ for $D_{MC} = 3.0$ and 4.0 μm. For extra soft particles, the maximum margination propensity reduces to $\overline{F}_M = 0.7$ found near $D_{MC} = 2.0$. At a larger $H_{ct} = 30\%$, stiff and soft particles appear to have very similar $\overline{F}_M$ trends beside some fluctuations. Maxima in $\overline{F}_M$ within the range between 0.8 and 1.0 are reached for $D_{MC} = 2.0$–3.0 μm. Also, in the arteriolar flow, the decrease in margination propensity for larger MC sizes ($D_{MC} > 3.0\ \mu$m) has to be ascribed to the effect of the lift force.

B. Implications in the rational design of blood-borne drug delivery systems

As discussed above, the dynamics of MCs in blood flow is regulated by the fine balance between the collision force originated from the presence of RBCs and the lift force, which can readily be estimated as described in Sec. III A. This fine balance is responsible for the occurrence of a maximum in margination efficiency which depends on the size and deformability of the particle as well as on the caliber and hematocrit of the considered blood vessel.

Small drug carriers, with a characteristic size $D_{MC} \leq 500$ nm, have generally a comparably low propensity to marginate, regardless of their deformability. This implies that small MCs with $D_{MC} \leq 500$ nm cannot efficiently exploit the process of margination, as already documented in several other studies,[15,18] and that their deformability does not have a substantial effect on the vascular transport of this small particles. Nevertheless, the size and deformability of small MCs do influence other transport processes, such as cell uptake and adhesion.[31,34,54]

Larger drug carriers ($D_{MC} > 500$ nm) exhibit a significant dependence of the margination propensity on MC size and deformability. Extra soft particles, whose deformability is similar to that of RBCs, marginate well only in the presence of a dense enough core of RBCs. At large hematocrits ($H_{ct} = 30\%$) in arterioles, the extra soft MCs reach a maximum in margination efficiency of $\overline{F}_M \sim 0.8$ for $D_{MC} = 3.0\ \mu$m. However, in capillaries, the extra soft particles possess a modest margination propensity of up to $\overline{F}_M \sim 0.4$ for $D_{MC} = 1.0$ and 2.0 μm at $H_{ct} = 30\%$. At lower hematocrits, which are often relevant in capillary flows, extra soft MCs mostly travel in the vessel center without interacting with the walls. Furthermore, stiff and soft MCs in this study show a similar behavior at large hematocrits ($H_{ct} = 30\%$) in arterioles. Large margination propensities up to $\overline{F}_M \sim 0.9$–1.0 are reached for $D_{MC} = 2.0\ \mu$m. For larger MC sizes, the lift force dominates and forces the particles into an intermediate zone between the CFL and the RBC-rich core. Similar observations can also be drawn for the stiff and soft MCs in capillaries. Here, a maximum in margination propensity up to $\overline{F}_M \sim 1.0$ is reached for $D_{MC} = 3.0\ \mu$m at $H_{ct} = 20\%$ and for $D_{MC} = 2.0\ \mu$m at $H_{ct} = 30\%$. Indeed, the higher is the hematocrit, the stronger are the collisions with RBCs, so that the maximum margination propensity is attained already for smaller MC sizes.

Based on these results, one of the main conclusions is that extra soft particles with their limited margination propensity and qualitative similarities to RBCs can be useful as vascular imaging agents in MR or CT. This is in line with the recent results, where RBCs were used as carriers.[31,33] On the other hand, the soft and stiff MCs with a size of about $D_{MC} \approx 2.0\ \mu$m marginate well in both arterioles and capillaries. Smaller carriers do not benefit enough from the collisions with RBCs, and often remain away from the walls. Larger carriers experience a strong lift force which significantly limits their margination.

C. Limitations of the margination analysis

Although the presented results have a clear physical interpretation and are in agreement with previous experimental and computational analyses, it is important to highlight main limitations that should be addressed in future studies. All simulations have been performed for a two-dimensional domain, because of the computational cost associated with the large set of independent parameters (5 MC sizes, three levels of MC deformability, two hematocrits, and two channel sizes). Especially, simulations in large vessels are very expensive for physiologically relevant hematocrit values, since a large number of RBCs is required and the spatial resolution of the flow is dictated by the size of MCs which are generally 2–7 times smaller than RBCs. Furthermore, simulations of particle margination in large vessels require very long simulation times, because lateral migration of MCs is slow. Despite the fact that the hydrodynamic interactions in 2D and 3D are different, the motion and migration of deformable RBCs and MCs are driven by similar physical mechanisms, and therefore, the margination propensity of different MCs is expected to be qualitatively similar in 2D and 3D. This is likely the reason for a good agreement between 2D and 3D models reported previously.[18]

Another factor that may affect the behavior of MCs in the microvascular flow is the viscosity ratio between the RBC cytosol and blood plasma, which is approximately equal to five. The viscosity ratio has an effect on the RBC dynamics[52,55] such that the tank-treading motion of the RBC membrane is suppressed by internal dissipation within the cytosol. Since the viscosity ratio affects the dynamics of single RBCs, it may change the migration of cells in the microvascular flow and alter the transport properties of MCs. Finally, further aspects which may be considered in future studies are the adhesion of MCs to the vessel

walls and the possible release of chemical compounds by the MCs. In addition to margination, the adhesion of MCs to vessel walls depends on the size and shape of MCs and the properties of adhesive interactions such as bond kinetic rates.[20,30] The release of chemical compounds from a particle in the blood flow has been simulated in a recent study[56] and would depend on the local flow advective and diffusive properties.

V. CONCLUSIONS

Two-dimensional mesoscopic simulations were employed to gain new insights in the vascular dynamics of carriers with different size and deformability. Simulations were conducted for two different classes of blood vessels: (i) capillaries with a channel height of 10 μm comparable to the RBC characteristic size and (ii) arterioles with a channel height of 50 μm. The model allowed us to systematically investigate the vascular behavior of MC with a size ranging from 0.5 to 4. 0 μm and different levels of deformability ranging from stiff to soft and extra soft particles, under different hematocrit conditions.

In a capillary flow, at physiologically relevant hematocrits, stiff and soft particles marginate efficiently toward the wall with the margination efficiency dependent on MC size. In addition to a few exceptions, margination occurs for nearly 100% of the particles with a size larger than 3 μm, while only 60% of the 1 μm MCs marginate. In contrast, extra soft particles experience a strong lift force that pushes them away from the wall, especially for particles with $D_{MC} > 3$ μm, resulting in poor margination. Smaller extra soft MC ($D_{MC} \leq 3$ μm) exhibit moderate margination propensity. Interestingly, at low hematocrits (<20%), which do occur in small vessels where the flow of RBC is confined, small MC become partially trapped within the bolus flow between consecutively moving RBC, while larger particles lead to a transient increase in the flow resistance through the disturbance of a train-like arrangement of RBC.

In arterioles, at physiologically relevant hematocrits of about 30%, margination efficiency of MC increases with the particle size up to $D_{MC} = 2$ μm, for which regardless of the particle deformability, over 80% of the MC do marginate. Indeed, the stiffer the particle, the more rapid the margination process takes place. Larger particles ($D_{MC} > 2$ μm) have a far more complex vascular dynamics, resulting from an interplay between the energetic collisions with the abundant and fast moving RBC and the lift force which grows with increasing MC size and deformability. The competition of these forces defines a maximum in margination propensity at $D_{MC} \approx 2$ μm for all tested deformability values. Note that this particle size corresponds to an efficient margination both in the smaller capillaries and arterioles.

In summary, sufficiently stiff and large MC ($D_{MC} > 1$ μm) marginate well both in small and large vessels, while very soft particles resemble the behavior of RBCs and exhibit moderate margination propensity only at large hematocrits. The vascular behavior of small particles ($D_{MC} < 0.5$ μm) is nearly unaffected by their deformability. The presented computational model can be used further to build design maps, identifying maxima in margination propensity for particles of various geometries (size and shape) and deformability levels under different flow conditions. These design maps are useful to instruct the rational selection of optimal MC for the delivery of therapeutic and imaging agents.

SUPPLEMENTARY MATERIAL

See the supplementary material for the results on near wall dynamics of a single RBC in a capillary flow, margination propensity for different choices of the skin-layer thickness, and tests of the microcarrier models.

ACKNOWLEDGMENTS

The authors acknowledge the financial support by the European Research Council, under the European Union's Seventh Framework Programme (Grant No. FP7/2007-2013) ERC CoG "POTENT" Grant Agreement No. 616695; the European Union's Horizon 2020 research and innovation programme under the Marie Skłodowska-Curie "MINDED" Grant Agreement No. 754490; and the Italian Ministry for Foreign Affairs (MAECI) for the Italy-Serbia Grant 2019, No. MAE005759. We also gratefully acknowledge the computing time granted through JARA on the supercomputer JURECA at Forschungszentrum Jülich.[57]

AUTHOR DECLARATIONS

Conflict of Interest

The authors have no conflicts to disclose.

Author Contributions

Wei Chien: Conceptualization (equal); Data curation (equal); Methodology (equal); Software (lead); Writing – original draft (equal); Writing – review & editing (equal). **Dmitry A. Fedosov:** Conceptualization (equal); Methodology (equal); Project administration (equal); Supervision (equal); Writing – original draft (equal); Writing – review & editing (equal). **Paolo Decuzzi:** Conceptualization (lead); Formal analysis (equal); Funding acquisition (lead); Methodology (equal); Project administration (lead); Supervision (lead); Writing – original draft (equal); Writing – review & editing (equal).

DATA AVAILABILITY

The data that support the findings of this study are available from the corresponding author upon reasonable request.

REFERENCES

[1]A. L. Palange, R. Palomba, I. F. Rizzuti, M. Ferreira, and P. Decuzzi, "Deformable discoidal polymeric nanoconstructs for the precise delivery of therapeutic and imaging agents," Mol. Ther. **25**, 1514 (2017).
[2]R. K. Jain and T. Stylianopoulos, "Delivering nanomedicine to solid tumors," Nat. Rev. Clin. Oncol. **7**, 653 (2010).
[3]T. J. Anchordoquy, Y. Barenholz, D. Boraschi, M. Chorny, P. Decuzzi, M. A. Dobrovolskaia, Z. S. Farhangrazi, D. Farrell, A. Gabizon, H. Ghandehari, B. Godin, N. M. La-Beck, J. Ljubimova, S. M. Moghimi, L. Pagliaro, J. H. Park, D. Peer, E. Ruoslahti, N. J. Serkova, and D. Simberg, "Mechanisms and barriers in cancer nanomedicine: Addressing challenges, looking for solutions," ACS Nano **11**, 12 (2017).
[4]M. Howard, B. J. Zern, A. C. Anselmo, V. V. Shuvaev, S. Mitragotri, and V. Muzykantov, "Vascular targeting of nanocarriers: Perplexing aspects of the seemingly straightforward paradigm," ACS Nano **8**, 4100 (2014).
[5]T. W. Secomb, "Blood flow in the microcirculation," Annu. Rev. Fluid Mech. **49**, 443 (2017).
[6]D. A. Fedosov, H. Noguchi, and G. Gompper, "Multiscale modeling of blood flow: From single cells to blood rheology," Biomech. Model. Mechanobiol. **13**, 239 (2014).

[7]T. M. Geislinger and T. Franke, "Hydrodynamic lift of vesicles and red blood cells in flow: From Fahraeus and Lindqvist to microfluidic cell sorting," Adv. Colloid Interface Sci. **208**, 161 (2014).
[8]J. B. Freund, "Numerical simulation of flowing blood cells," Annu. Rev. Fluid Mech. **46**, 67 (2014).
[9]D. A. Fedosov, J. Fornleitner, and G. Gompper, "Margination of white blood cells in microcapillary flow," Phys. Rev. Lett. **108**, 028104 (2012).
[10]M. J. Pearson and H. H. Lipowsky, "Influence of erythrocyte aggregation on leukocyte margination in postcapillary venules of rat mesentery," Am. J. Physiol. **279**, H1460 (2000).
[11]J. B. Freund, "Leukocyte margination in a model microvessel," Phys. Fluids **19**, 023301 (2007).
[12]D. A. Reasor, Jr., M. Mehrabadi, D. N. Ku, and C. K. Aidun, "Determination of critical parameters in platelet margination," Ann. Biomed. Eng. **41**, 238 (2013).
[13]H. Zhao and E. S. G. Shaqfeh, "Shear-induced platelet margination in a microchannel," Phys. Rev. E **83**, 061924 (2011).
[14]G. Závodszky, B. van Rooij, B. Czaja, V. Azizi, D. de Kanter, and A. G. Hoekstra, "Red blood cell and platelet diffusivity and margination in the presence of cross-stream gradients in blood flows," Phys. Fluids **31**, 031903 (2019).
[15]T. R. Lee, M. Choi, A. M. Kopacz, S. H. Yun, W. K. Liu, and P. Decuzzi, "On the near-wall accumulation of injectable particles in the microcirculation: Smaller is not better," Sci. Rep. **3**, 2079 (2013).
[16]H. Ye, Z. Shen, L. Yu, M. Wei, and Y. Li, "Manipulating nanoparticle transport within blood flow through external forces: An exemplar of mechanics in nanomedicine," Proc. Math. Phys. Eng. Sci. **474**, 20170845 (2018).
[17]P. Charoenphol, P. J. Onyskiw, M. Carrasco-Teja, and O. Eniola-Adefeso, "Particle-cell dynamics in human blood flow: Implications for vascular-targeted drug delivery," J. Biomech. **45**, 2822 (2012).
[18]K. Muller, D. A. Fedosov, and G. Gompper, "Margination of micro- and nanoparticles in blood flow and its effect on drug delivery," Sci. Rep. **4**, 4871 (2014).
[19]Z. Liu, J. R. Clausen, R. R. Rao, and C. K. Aidun, "A unified analysis of nano-to-microscale particle dispersion in tubular blood flow," Phys. Fluids **31**, 081903 (2019).
[20]K. Vahidkhah and P. Bagchi, "Microparticle shape effects on margination, near-wall dynamics and adhesion in a three-dimensional simulation of red blood cell suspension," Soft Matter **11**, 2097 (2015).
[21]K. Sinha and M. D. Graham, "Shape-mediated margination and demargination in flowing multicomponent suspensions of deformable capsules," Soft Matter **12**, 1683 (2016).
[22]P. Lenarda, A. Coclite, and P. Decuzzi, "Unraveling the vascular fate of deformable circulating tumor cells via a hierarchical computational model," Cel. Mol. Bioeng. **12**, 543 (2019).
[23]K. Muller, D. A. Fedosov, and G. Gompper, "Understanding particle margination in blood flow: A step toward optimized drug delivery systems," Med. Eng. Phys. **38**, 2 (2016).
[24]R. D'Apolito, G. Tomaiuolo, F. Taraballi, S. Minardi, D. Kirui, X. Liu, A. Cevenini, R. Palomba, M. Ferrari, F. Salvatore, E. Tasciotti, and S. Guido, "Red blood cells affect the margination of microparticles in synthetic microcapillaries and intravital microcirculation as a function of their size and shape," J. Control Release **217**, 263 (2015).
[25]F. Gentile, C. Chiappini, D. Fine, R. C. Bhavane, M. S. Peluccio, M. M. Cheng, X. Liu, M. Ferrari, and P. Decuzzi, "The effect of shape on the margination dynamics of non-neutrally buoyant particles in two-dimensional shear flows," J. Biomech. **41**, 2312 (2008).
[26]S. Y. Lee, M. Ferrari, and P. Decuzzi, "Shaping nano-/micro-particles for enhanced vascular interaction in laminar flows," Nanotechnology **20**, 495101 (2009).
[27]P. Decuzzi and M. Ferrari, "The adhesive strength of non-spherical particles mediated by specific interactions," Biomaterials **27**, 5307 (2006).
[28]G. Adriani, M. D. de Tullio, M. Ferrari, F. Hussain, G. Pascazio, X. Liu, and P. Decuzzi, "The preferential targeting of the diseased microvasculature by disk-like particles," Biomaterials **33**, 5504 (2012).
[29]A. L. van de Ven, P. Kim, O. Haley, J. R. Fakhoury, G. Adriani, J. Schmulen, P. Moloney, F. Hussain, M. Ferrari, X. Liu, S. H. Yun, and P. Decuzzi, "Rapid tumoritropic accumulation of systemically injected plateloid particles and their biodistribution," J Control Release **158**, 148 (2012).
[30]M. Cooley, A. Sarode, M. Hoore, D. A. Fedosov, S. Mitragotri, and A. Sen Gupta, "Influence of particle size and shape on their margination and wall-adhesion: Implications in drug delivery vehicle design across nano-to-micro scale," Nanoscale **10**, 15350 (2018).
[31]T. J. Merkel, S. W. Jones, K. P. Herlihy, F. R. Kersey, A. R. Shields, M. Napier, J. C. Luft, H. Wu, W. C. Zamboni, A. Z. Wang, J. E. Bear, and J. M. DeSimone, "Using mechanobiological mimicry of red blood cells to extend circulation times of hydrogel microparticles," Proc. Natl. Acad. Sci. U. S. A. **108**, 586 (2011).
[32]P. M. Glassman, E. D. Hood, L. T. Ferguson, Z. Zhao, D. L. Siegel, S. Mitragotri, J. S. Brenner, and V. R. Muzykantov, "Red blood cells: The metamorphosis of a neglected carrier into the natural mothership for artificial nanocarriers," Adv. Drug Delivery Rev. **178**, 113992 (2021).
[33]C. H. Villa, A. C. Anselmo, S. Mitragotri, and V. Muzykantov, "Red blood cells: Supercarriers for drugs, biologicals, and nanoparticles and inspiration for advanced delivery systems," Adv. Drug Delivery Rev. **106**, 88 (2016).
[34]R. Palomba, A. L. Palange, I. F. Rizzuti, M. Ferreira, A. Cervadoro, M. G. Barbato, C. Canale, and P. Decuzzi, "Modulating phagocytic cell sequestration by tailoring nanoconstruct softness," ACS Nano **12**, 1433 (2018).
[35]M. B. Fish, C. A. Fromen, G. Lopez-Cazares, A. W. Golinski, T. F. Scott, R. Adili, M. Holinstat, and O. Eniola-Adefeso, "Exploring deformable particles in vascular-targeted drug delivery: Softer is only sometimes better," Biomaterials **124**, 169 (2017).
[36]A. D. Grief and G. Richardson, "Mathematical modelling of magnetically targeted drug delivery," J. Magn. Magn. Mater. **293**, 455 (2005).
[37]F. Garello, Y. Svenskaya, B. Parakhonskiy, and M. Filippi, "Micro/nanosystems for magnetic targeted delivery of bioagents," Pharmaceutics **14**, 1132 (2022).
[38]M. Lee, A. Shelke, S. Singh, J. Fan, P. Zaleski, and S. Afkhami, "Numerical simulation of superparamagnetic nanoparticle motion in blood vessels for magnetic drug delivery," Phys. Rev. E **106**, 015104 (2022).
[39]J. J. Monaghan, "Smoothed particle hydrodynamics," Rep. Prog. Phys. **68**, 1703 (2005).
[40]K. Tsubota and S. Wada, "Effect of the natural state of an elastic cellular membrane on tank-treading and tumbling motions of a single red blood cell," Phys. Rev. E Stat., Nonlinear, Soft Matter Phys. **81**, 011910 (2010).
[41]F. V. T. Kruger and D. Raabe, "Efficient and accurate simulations of deformable particles immersed in a fluid using a combined immersed boundary lattice Boltzmann finite element method," Comput. Math. Appl. **61**, 3485 (2010).
[42]W. Strychalski, C. A. Copos, O. L. Lewis, and R. D. Guy, "A poroelastic immersed boundary method with applications to cell biology," J. Comput. Phys. **282**, 77 (2015).
[43]C. S. Peskin, "The immersed boundary method," Acta Numer. **11**, 479 (2002).
[44]S. Plimpton, "Fast parallel algorithms for short-range molecular dynamics," J. Comput. Phys. **117**, 1 (1995).
[45]S. J. Lind, R. Xu, P. K. Stansby, and B. D. Rogers, "Incompressible smoothed particle hydrodynamics for free-surface flows: A generalised diffusion-based algorithm for stability and validations for impulsive flows and propagating waves," J. Comput. Phys. **231**, 1499 (2012).
[46]S. Litvinov, M. Ellero, X. Y. Hu, and N. A. Adams, "A splitting scheme for highly dissipative smoothed particle dynamics," J. Comput. Phys. **229**, 5457 (2010).
[47]T. Ye, N. Phan-Thien, C. T. Lim, L. Peng, and H. Shi, "Hybrid smoothed dissipative particle dynamics and immersed boundary method for simulation of red blood cells in flows," Phys. Rev. E **95**, 063314 (2017).
[48]Q. M. Qi and E. S. G. Shaqfeh, "Theory to predict particle migration and margination in the pressure-driven channel flow of blood," Phys. Rev. Fluids **2**, 093102 (2017).
[49]D. Barthès-Biesel, "Motion and deformation of elastic capsules and vesicles in flow," Annu. Rev. Fluid Mech. **48**, 25 (2016).
[50]G. Tomaiuolo, L. Lanotte, G. Ghigliotti, C. Misbah, and S. Guido, "Red blood cell clustering in Poiseuille microcapillary flow," Phys. Fluids **24**, 051903 (2012).
[51]D. Katanov, G. Gompper, and D. A. Fedosov, "Microvascular blood flow resistance: Role of red blood cell migration and dispersion," Microvasc. Res. **99**, 57 (2015).

[52]W. Chien, G. Gompper, and D. A. Fedosov, "Effect of cytosol viscosity on the flow behavior of red blood cell suspensions in microvessels," Microcirculation **28**, e12668 (2021).
[53]N. Takeishi and Y. Imai, "Capture of microparticles by bolus flow of red blood cells in capillaries," Sci. Rep. **7**, 5381 (2017).
[54]A. C. Anselmo and S. Mitragotri, "Impact of particle elasticity on particle-based drug delivery systems," Adv. Drug Delivery Rev. **108**, 51 (2017).
[55]D. Agarwal and G. Biros, "Shape dynamics of a red blood cell in Poiseuille flow," Phys. Rev. Fluids **7**, 093602 (2022).
[56]B. Kaoui, "Computer simulations of drug release from a liposome into the bloodstream," Eur. Phys. J. E **41**, 20 (2018).
[57]J. S. Centre, "JURECA: Data Centric and Booster Modules implementing the Modular Supercomputing Architecture at Jülich Supercomputing Centre," J. Large-Scale Res. Facil. **7**, A182 (2021).